JOURNAL OF MATERIALS SCIENCE **39** (2004) 73–84

The effect of the reduction of carbon content on the toughness of high chromium white irons in the as-cast state

A. KOOTSOOKOS
School of Aerospace Mechanical and Manufacturing Engineering, RMIT University, GPO Box 2476V, Melbourne 3001, Australia
E-mail: alex.kootsookos@ems.rmit.edu.au

J. D. GATES
UQ Materials Performance, Frank White Building, The University of Queensland, St. Lucia 4072, Australia

Three high chromium white cast irons were examined in the as-cast state to determine the effect of the carbon content on the fracture toughness. The plane strain fracture toughness K_{Ic} and the fracture strength were measured for each alloy. X-ray mapping was used to identify the phases on the fracture surfaces. Scanning electron fractography and optical microscopy were used to determine the volume fraction of each phase on the fracture surfaces. It was found that most fracture occurred in the eutectic carbides, but that for the alloys with a reduced volume fraction of eutectic carbides, a small amount of crack propagation occurred in the austenitic dendrites. This change in crack path correlated with an increase in fracture toughness. The Ritchie-Knott-Rice model of brittle fracture was applied. It was found to sensibly predict the critical length for fracture for each alloy. Deep etching was employed to examine the distribution of eutectic carbides. It was found that the eutectic carbides formed a continuous network in each case.

1. Introduction

Traditionally, high chromium white cast irons have been used in applications where high wear resistance is required [1]. In modern mining applications, alloys used in crushing and grinding operations need a combination of toughness and wear resistance [1, 2]. Current white irons, while exhibiting excellent wear properties have low fracture toughnesses and are only used in those applications where a limited amount of impact occurs [1]. If the toughness of these alloys could be improved, then use of them in high impact applications will result in better materials usage and a reduction in down time due to their high abrasion resistance [3].

High chromium white irons are typically cast as hypoeutectic alloys having a primary phase of dendritic austenite with the eutectic made up of austenite and M_7C_3 carbides [4]. The eutectic carbides form a continuous three-dimensional network within the interdendritic spaces [5]. During cooling from the melt, the eutectic austenite transforms to martensite [4, 5]. The final as-cast alloy has three constituents: dendritic austenite, eutectic austenite and/or martensite, and eutectic carbides.

Fractographic studies and failure theories have generally ignored the presence of the eutectic iron [6, 7]. Durman [7] and Zum Gahr [6] both found that the eutectic carbides dominated the fracture surfaces. They also observed small amounts of fracture through a second phase, but differed in their interpretations of this feature. Durman claimed it exhibited features typical of strain-induced martensite, while Zum Gahr classified it as failure through the dendritic matrix [6, 7]. Work done by Hann and Gates has shown that some cast irons do exhibit a transformation toughening reaction, but not generally in the as-cast condition where the martensite start temperature (M_s) is far below room temperature [4]. Neither Durman or Zum Gahr make any comment regarding the eutectic iron which forms the matrix of the eutectic microconstituents. This phase is likely to be at least partially martensitic [4] and would therefore provide a low energy crack path which should be visible on the fracture surfaces.

Currently, the only reliable conclusion which can be drawn from fractographic studies is that the toughness of high chromium white irons in the as-cast state is limited by the extreme brittleness of the eutectic carbides.

The most promising avenue for improving toughness is to force the crack to propagate through the dendritic constituent more frequently. The most obvious way of forcing the crack into the dendrites is to reduce the continuity of the eutectic carbide network.

In this vein, much work has been done to find an inoculating agent for the eutectic carbides with little

success [3, 8–10]. High temperature heat treatments have also been used to "spheroidize" the eutectic carbides. While such treatments do produce improvements in toughness, they are too costly to be commercially viable [9, 10].

Other researchers have reduced the volume fraction of eutectic carbides in an effort to reduce the continuity of the carbide network [7, 11]. Maratray [12] showed that the carbon and chromium contents control the volume fraction of eutectic carbides according to the following equation:

$$\%\text{E.C.} = 12.33(\%\text{C}) + 0.55(\%\text{Cr}) - 15.2 \quad (1)$$

where, %E.C. is the volume percent of eutectic carbides, %C is the weight percent carbon, and %Cr is the weight percent chromium.

The major aims of this research were:

(i) to produce unambiguous identification of the phases present on the fracture surfaces and to resolve contradictory interpretations in the literature;
(ii) to assess the effect of reduction in carbon content on the volume fraction of eutectic carbides;
(iii) to assess the effect of reduction of carbon content on the fracture toughness of high chromium white irons in the as-cast state;
(iv) to determine whether increases in fracture toughness can be related to crack path for the as-cast material; and
(v) to apply the Ritchie-Knott-Rice model [13] (hereafter RKR) to define the process of crack propagation for a 1.9%C iron.

2. Experimental

2.1. Alloys

Three alloys of different carbon contents were examined (see Table I). Alloy A was designed according to the Australian standard for a 20-2-1 Cr-Mo white iron [14]. The other alloys are "reduced carbon" white irons, and were designed with the intention of determining the effect of reducing carbon content on toughness. Casts B, C and D have the same nominal composition and can be considered the same alloy.

Other deliberate variations were in the molybdenum, nickel and silicon levels. Each of these elements must be controlled to achieve the required hardenability [12, 14, 15]. In the case of the current study, each alloy was designed to achieve a through-thickness hardenability in an industrial sized casting, even though the experiments used only laboratory sized castings.

Hardenability in high chromium white cast iron is known to be reduced by increasing the carbon and silicon contents [12, 15]. Increasing molybdenum and nickel off sets these effects [14, 17]. Thus alloy A with the highest carbon content required an increased molybdenum level. This alloy was designed to conform to the relevant standard, and therefore had to contain silicon and nickel weight percentages of not more than 1% in each case [14].

The reduced-carbon alloys, B and E were designed with higher than typical silicon contents because results in the literature indicated that an increased silicon content improved the fracture toughness of high chromium white iron [16].

It has also been found that increased silicon promotes the formation of pearlite [17]. Norman [15] showed that increased nickel counteracted this effect of silicon. Alloys B and E were designed accordingly and have higher nickel contents than that recommended by the standard specifications.

After casting, each of the alloys were given a triple heat treatment at 200°C for two hours. It has been thought that this treatment tempers the eutectic iron [18].

TABLE I Alloys examined in this study. Deliberate variations in composition are in bold

Alloy	**Cr**	**C**	**Mo**	**Ni**	**Si**	Mn	Cu	V	S	P
A	**18.7**	**2.82**	**2.59**	**1.1**	**0.7**	1.04	1.00	0.42	0.008	0.023
B	**18.2**	**1.86**	**1.93**	**1.54**	**1.2**	1.13	0.94	0.53	0.007	0.023
C	**18.85**	**1.89**	**1.83**	**1.59**	**1.22**	1.03	0.99	0.40	N.A	N.A
D	**17.4**	**1.86**	**1.76**	**1.77**	**1.25**	0.96	1.0	0.34	0.018	0.017
E	**18.9**	**1.52**	**1.75**	**1.60**	**1.16**	0.98	0.94	0.48	0.011	0.017
F	**14.6**	**1.43**	**0.7**	**0.1**	**0.57**	0.85	0.02	0.25	0.005	0.027

2.2. Mechanical testing

The plane strain fracture toughness, K_{Ic}, of all alloys was measured in accordance with ASTM E-399 [19]. Four tests were done for each alloy in the as-cast $+3 \times 200$ state.

A blunt-notch, three point bend test was used as a measure of the fracture strength. Specimens used in this test were of dimensions $10 \times 10 \times 55$ mm with an average notch depth of 2.5 mm and an average notch root radius of 0.85 mm. The notch root radii varied by ± 0.2 mm and the notch depth varied by ± 0.1 mm. The support span used was 40 mm, with a cross-head speed of 2 mm/min. At least five tests were performed for each alloy.

Tensile tests were performed using a screw-driven Instron, with a cross-head speed of 0.5 mm/min. For alloy B, double-shoulder cylindrical specimens were used, similar to Houndsfield "E", but with a larger gauge section of 50 mm^2. From these tests 0.1% proof stresses were calculated. No tensile bars of alloy E (1.5%C) were available, so an estimate of the yield strength of this material was made by averaging the results for alloy B (1.8%C) and alloy F (1.43%C).Tensile testing of alloy F was performed using small Houndsfield "A" specimens (see Fig. 1). Yield strength information for standard 20-2-1 irons such as alloy A is available in the literature [20], so no tensile testing of this alloy was performed.

2.3. Metallography and fractography

The volume fraction of eutectic carbides was determined using manual point counting techniques. Three mutually perpendicular views were examined for each

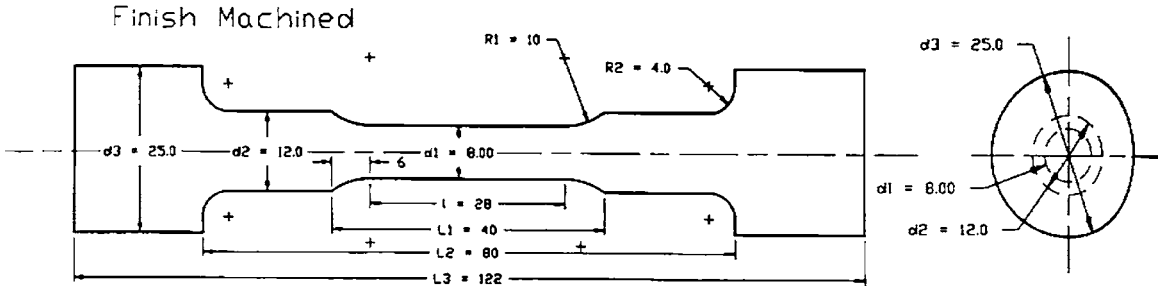

Figure 1 Geometry of tensile samples used to determine the tensile properties of alloy B. Alloy F tensile bars had the same geometry, but dimensions of d3 = 7.6 mm, d2 = 4.9 mm, d1 = 3.6 mm, l = 12.6 mm, L_1 = 14.6 mm, L_2 = 21.7 mm, L_3 = 28.4 mm. All rounding radii were 1 mm.

casting, with fifty fields measured for each view [21, 22].

Double-sided crack path samples were prepared and examined using optical microscopy. These specimens were cross-sections through intact K_{Ic} bars. The cross sections were taken from the plane strain region of the bar and were cut using a water-cooled abrasive wheel. The samples were then polished and mounted using standard metallographic techniques. A Quanti-Met 670 was used to measure the linear proportion of cracking through the dendrites.

For scanning electron fractography, fracture surfaces were cut using a water-cooled abrasive cut-off wheel. The fracture surfaces were then cleaned in acetone, dried and mounted. Secondary electron images were recorded from regions where plane strain conditions existed during testing.

To identify the different phases on the fracture surfaces energy dispersive spectrographic (EDS) X-ray maps were made of an alloy B fracture surface. Maps of Cr K_α and Fe K_α lines were recorded. The magnification used for this was $\times$500 with an accelerating voltage of 10 kV.

The areal fraction of cracking through the eutectic matrix was determined by point-counting. Thirty different views were used. A circular grid was applied to each view in the point counting process to counteract any preferred orientation of the fracture surface [22]. Following ASTM E562-89 [23], spacing of the grid points was such that two successive points could not lie in the same area of interest.

The thickness of the eutectic phases was measured using manual quantitative metallography. For each material, twenty fields were taken on three mutually perpendicular sections.

Deep-Etching was performed by suspending polished samples in a solution of: 154 mL ethanol, 6 mL HCL, 20 mL HNO_3, and $FeCl_3$ (added to saturation).

The solution was stirred and the samples were etched for 40 min [26].

3. Results and discussion

3.1. Microstructure

The structures of A, B and E are shown in Figs 2, 3 and 4, below. It can be seen that for the reduced-carbon alloys B and E, the dendritic structure is more pronounced and the eutectic carbide rods and blades appear to be finer than in the full carbon alloy A. Close examination of Figs 2–4 shows shadowing around the eutectic carbides. This is probably indicative of the presence of eutectic martensite, consistent with Hann's transmission electron results [4].

Quantitative metallography used to determine the volume fraction of eutectic carbides, showed a reasonable agreement with Maratray's formula (Equation 1, Table II). Other researchers have suggested that Maratray's formula may not always be reliable [1].

Deep etching of the samples was performed to see if reduction of the carbon content altered the continuity of the eutectic carbides. As can be seen from Figs 5, 6

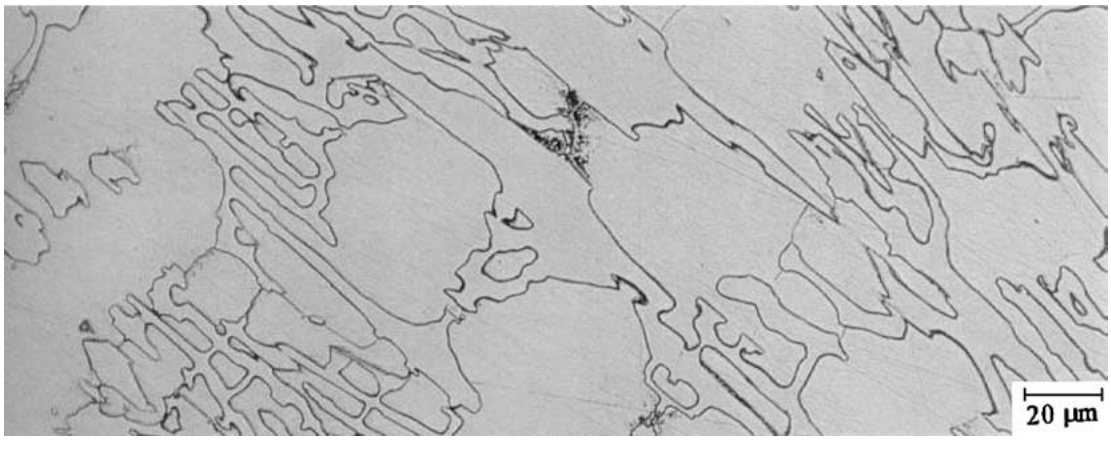

Figure 2 Light reflected micrograph of alloy A in the ascast and tempered state. Note the eutectic carbide structure.

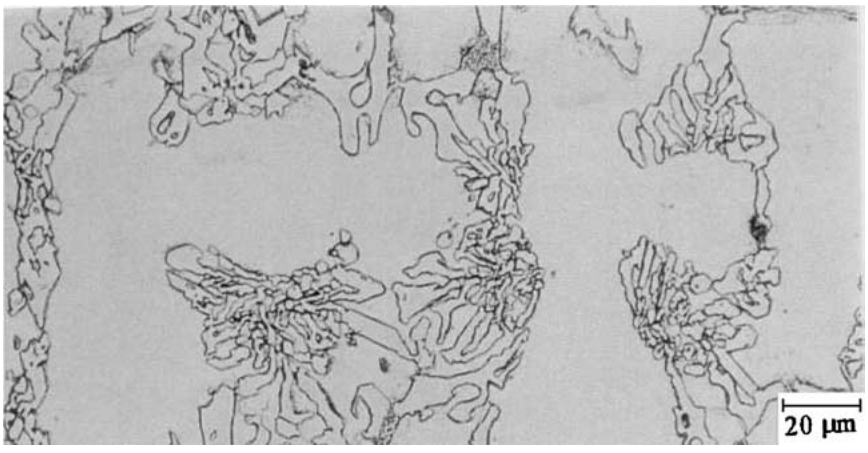

Figure 3 Light reflected micrograph of alloy B in the ascast and tempered state. Note that the dendritic structure is more obvious here.

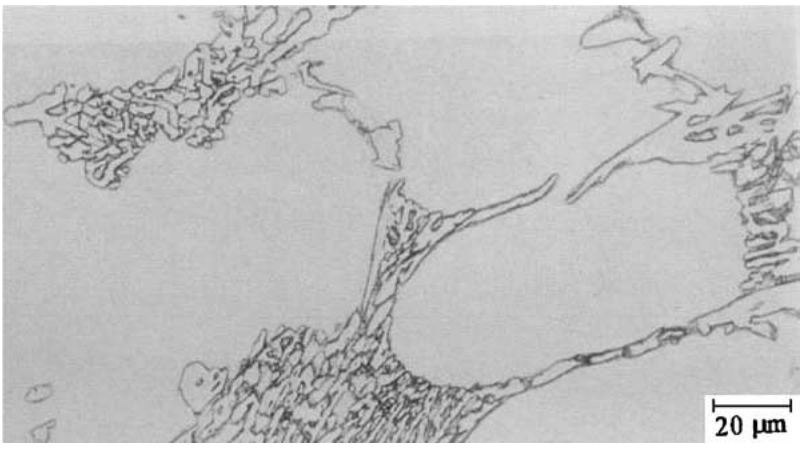

Figure 4 Light reflected micrograph of alloy F in the ascast and tempered state. Note the fine structure.

and 7, even for the lowest carbon content the eutectic carbides still formed a continuous network.

These observations are consistant with Powell [5] and others [25] who have shown that reduction of the carbon content of high chromium white irons does not alter the continuity of the eutectic carbide network.

3.2. Mechanical properties

The K_{Ic} results in Table III show that there is a significant improvement in fracture toughness when the carbon content is reduced. In an earlier paper by the authors [11], it is shown that these results fit well within the scatter band of the published data, confirming the idea that reduction of carbon content improves the as-cast toughness.

Table III also lists the values of the blunt notch fracture strength, σ_F^{blunt}. Calculation of this quantity used the slip-line field theory [26]:

$$\sigma_F^{blunt} = \sigma_{max} = 2k\left(1 + \ln\left(1 + \frac{x}{r}\right)\right) \qquad (2)$$

where σ_{max} = the maximum stress below the notch at fracture, k = the uniaxial shear strength = $\sigma_y/2$ for a Tresca solid, x = the size of the plastic zone, and r = root radius of the notch.

The shear strength for each material was determined using the proof stress results from the tension tests and assuming that the materials behaved as Tresca solids [27]. The size of the plastic zone was calculated with the peak loads measured in the blunt-notch test and the finite-element analysis published by Griffiths and Owen (1971) [26]. The root radius for each sample was measured using a profilometer.

The slip-line field theory assumes that the maximum stress ahead of a crack tip is at the elastic-plastic

TABLE II Maratray's formula (Equation 1) predicts the volume fraction of eutectic carbides quite accurately, for the carbon contents examined

Alloy	C (wt%)	Cr (wt%)	Vol% eutectic carbides (measured)	Vol% eutectic carbides (Equation 1)
A	2.82	18.7	27 ± 4	29.9
B	1.86	18.2	21 ± 6	17.7
F	1.52	18.9	14 ± 4	12.8

TABLE III As-cast mechanical property results

Alloy	wt% carbon	Vol% eutectic carbides (measured)	K_{Ic} (MPa$\sqrt{m}$)	σ_y (MPa)	σ_F^{blunt} (MPa)	$\sigma_F^{blunt}/\sigma_y$ (MPa)
A	2.82	27	25.6 ± 1.4	1010	1053 ± 11	1.0 ± 0.01
B	1.86	21	28.5 ± 0.9	595	735 ± 21	1.2 ± 0.04
E	1.52	14	32.1 ± 2.1	572	738 ± 17	1.3 ± 0.03

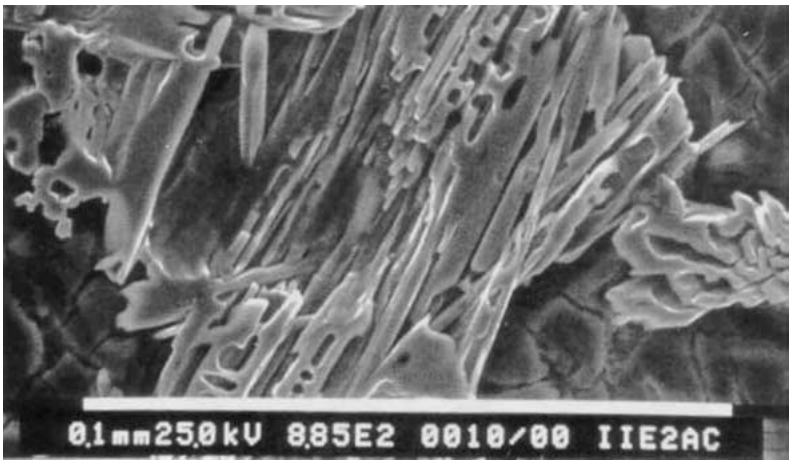

Figure 5 Alloy A, 2.82%C, 27 vol% eutectic carbides Deep Etching reveals the continuous nature of the eutectic carbide network.

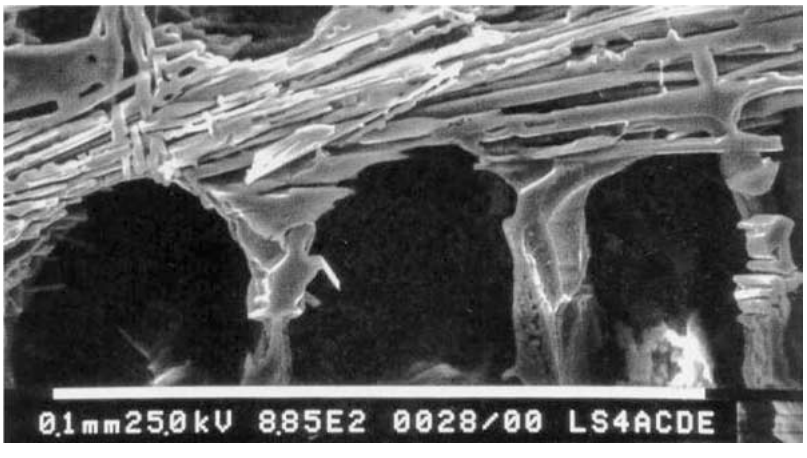

Figure 6 Alloy B, 1.86%C, 21 vol% eutectic carbides Deep Etched reduced carbon alloy, showing that the eutectic carbides are still continuous.

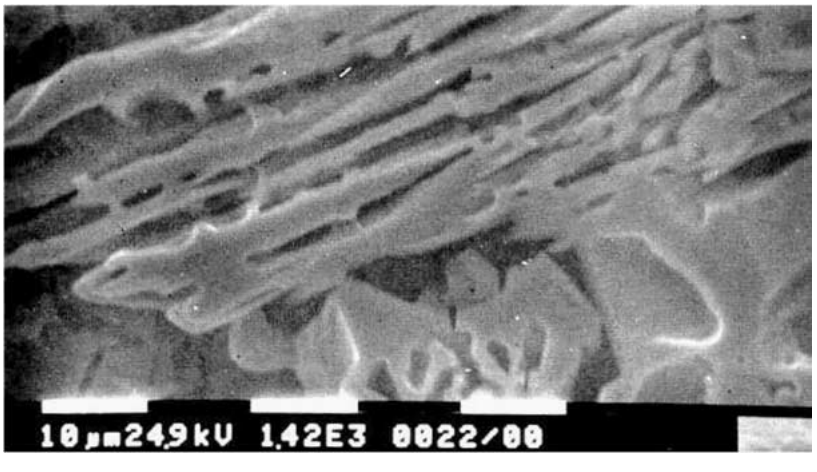

Figure 7 Alloy E, 1.5%C, 14 vol% eutectic carbides. Deep Etching demonstrates that the alloy with the lowest carbon content still has a continuous eutectic carbide network.

interface [28]. Researchers using finite-element analysis have found that this is not always the case [26]. However, as no correct elastic-plastic stress distribution for the geometry used is currently available, slip-line field theory provides the best estimate of the fracture strength.

Consideration of Equation 2 shows that σ_F^{blunt} is dependant on both the yield strength of the material and the size of the plastic zone at fracture. This means that high σ_F^{blunt} values can occur for two different reasons:

(a) the yield strength is high (i.e., the material is strong)

(b) a large amount of plastic deformation occurs before fracture (i.e., the material is tough).

For example, A exhibits the highest σ_F^{blunt} value because it has a high yield strength. Alloys E and B have the same values of σ_F^{blunt}, but for alloy E, the σ_F^{blunt} value

TABLE IV Measurement of the amount of crack propagation through the dendrites

Alloy	Vol% eutectic carbides	%carbon	K_{Ic} (MPa$\sqrt{m}$)	σ_y (MPa)	σ_F^{blunt} (MPa)	$\sigma_F^{blunt}/\sigma_y$ (MPa)	% crack path through the dendrites
A	27	2.82	25.6	1010	1053	1.04	0.13 ± 0.18
B	21	1.86	28.5	595	735	1.24	4.8 ± 0.8
E	14	1.52	32.1	572	738	1.29	3.6 ± 1.9

is produced by the greater amount of plastic deformation compared to B, whereas alloy B has the higher yield strength. Thus, the relative toughnesses of the alloys cannot be assessed on the basis of σ_F^{blunt} alone. However, consideration of the stress field ahead of a crack shows that the ratio of σ_F^{blunt} to σ_y provides a measure of relative ductility.

To demonstrate this, consider that at the tip of a crack, applied tensile stresses are intensified. Brittle fracture occurs when a critical stress, the fracture stress σ_F, is achieved locally in the region near the crack tip. However, if the local flow stress σ_o is less than σ_F, plastic deformation will occur first creating a plastic zone around the crack tip. The fracture stress σ_F can then only be exceeded if work hardening occurs.

Thus, the amount of plastic deformation which occurs prior to fracture depends on the relative values of σ_o and σ_F. When the ratio of σ_F/σ_o is close to 1, little plastic deformation and work-hardening must occur for the fracture stress to be exceeded, resulting in a limited amount of energy absorption before catastrophic fracture. In this case the ductility is also expected to be limited. As the ratio σ_F/σ_o increases, more work-hardening and plastic deformation must occur before catastrophic fracture, resulting in more energy being absorbed during fracture and a greater ductility. In the extreme case where σ_F/σ_o is very high, the material in the plastic zone cannot reach σ_F by work-hardening and the failure becomes ductile, being achieved by the attainment of a critical *strain* rather than a critical *stress* [29].

The flow stress σ_o and the fracture stress σ_F are local stresses which cannot be measured directly, but can be estimated by macroscopic properties. Throughout this study, the flow stress was estimated by the uniaxial yield strength, σ_y and the fracture stress is estimated by σ_F^{blunt}. Thus the ratio of σ_F^{blunt} to σ_y can be used as a measure of the ductility of different alloys. This ratio is also of importance when developing a model for the fracture of white irons.

Since measurement of σ_F^{blunt} was made using specimens which were not pre-cracked, the ratio $\sigma_F^{blunt}/\sigma_y$ must reflect the amount of plastic deformation associated with both crack initiation and crack propagation. In contrast K_{Ic}, being measured from specimens with sharp pre-cracks, gives an indication of the energy associated with crack propagation only. Comparison of the percentage change in K_{Ic} and $\sigma_F^{blunt}/\sigma_y$ with reducing carbon content shows that both quantities improve by approximately the same percentage. Thus, most of the improvement in toughness is due to increases in the amount of energy associated with crack propagation rather than crack initiation.

3.3. Crack path analysis

Image analysis of double-sided crack path specimens was used to measure the proportions of cracking through the different phases. Initially, the crack path was classified into dendritic and eutectic cracking, as the precise path of fracture within the eutectic "packets" was difficult to discern.

The results in Table IV indicate that as the carbide volume fraction is reduced, both the fracture toughness and the ratio $\sigma_F^{blunt}/\sigma_y$ increase by approximately 25%. This increase in fracture toughness is accompanied by an alteration of the crack path with the two reduced carbon alloys (B and E) exhibiting more crack propagation through the austenitic dendrites. The large scatter associated with the crack path measurement of E means that there can be no differentiation between the two reduced-carbon alloys in terms of the percentage of crack propagation through the dendrites.

Since cracking through the austenitic dendrites would require more energy than fracture of the eutectic packets (carbide and martensite) it can be concluded that the increased amount of crack propagation through the dendrites is responsible for the improved fracture toughness of the reduced carbon alloys.

Durman [7] examined a range of alloys with varying carbon contents and found that a reduction in the volume fraction of eutectic carbides increased the amount of crack propagation through the dendrites. He attributed this change in the crack path to a discontinuous network of eutectic carbides at low carbon contents and the ability of the austenitic dendrites to transform to martensite.

Deep etching of the alloys A, B and E showed that the eutectic carbides are continuous even at low carbon contents (Figs 5–7). Results from Hann and Gates [4] indicate that alloys B and E should have an M_s well below room temperature, implying that strain induced martensite could not be produced. This implies that in the reduced carbon alloys, the crack is forced into the austenitic dendrites.

Zum Gahr [6] claimed to have observed cracking though the austenitic dendrites, however he ignored the presence of the eutectic martensite. He also only examined full carbon alloys. The results from Table IV indicate that cracking through the austenitic dendrites is very rare in full carbon alloys.

3.4. Identification of the different phases on the fracture surfaces

Fig. 8 is a secondary electron image, showing a typical region of the fracture surface of alloy B. Fracture through two different phases is evident. Area A, which is shown at higher magnification in Fig. 9, is classical

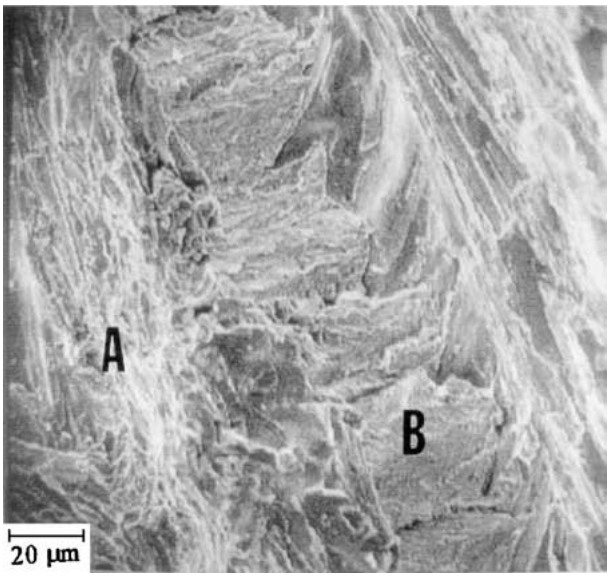

Figure 8 Fracture surface which was X-ray mapped (Secondary Electron Image).

cleavage fracture that would conventionally be interpreted as fracture through the brittle eutectic carbides. Area B, shown in Fig. 10, can be denoted as quasi-cleavage. It is this phase which Zum Gahr described as failure of the dendrites, and which Durman assumed represented fracture of strain-induced martensite (SIM) in the dendrites [6, 7]. Results from Hann and Gates [4] indicate that alloy B should have a martensitic start temperature below—196°C and therefore, no SIM could form at room temperature.

Figs 11 and 12 show Cr K_α and Fe K_α X-ray maps of Fig. 8. Region A is illuminated strongly in the chromium map, confirming that this is fracture through the Cr-rich eutectic carbides. Region B is more obvious in the iron map, indicating it could be either the dendrites or the eutectic matrix phase. The observed quasi-cleavage fracture mode is more characterisitc of eutectic martensite than dendritic austenite, although it is difficult to predict the fracture mode of a face-centred cubic material within a more brittle structure loaded under highly constrained conditions.

Further evidence that the quasi-cleavage failure in region B represents eutectic martensite rather than dendritic austenite lies in the fact that this type of failure was observed more frequently in the full carbon alloy A than in the reduced carbon alloys (Table V).

By comparison, the double-sided crack path studies showed that cracking through dendrites is rare even in the lower carbon alloys (Table IV). Clearly then the quasi-cleavage areas cannot represent cracking though dendrites. Region B must be cracking through the eutectic matrix, and region A cracking through the eutectic carbides.

Failure through the austenitic dendrites was identified from a double-sided crack path specimen. The sample was photographed while still intact (Fig. 13). After

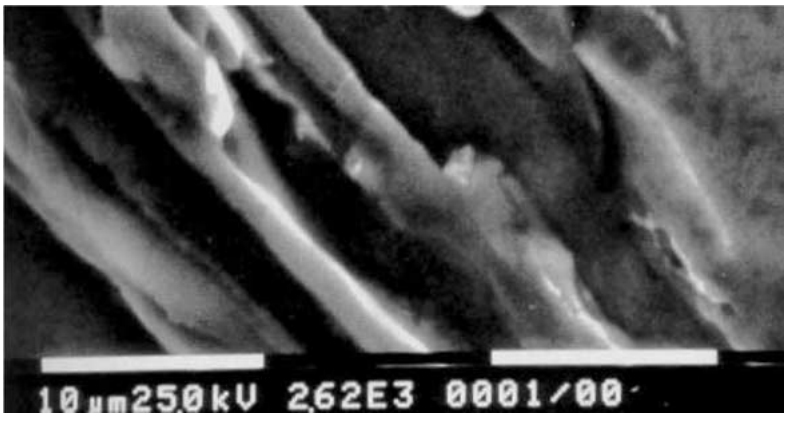

Figure 9 Secondary Electron image of Area A, showing classical cleavage fracture.

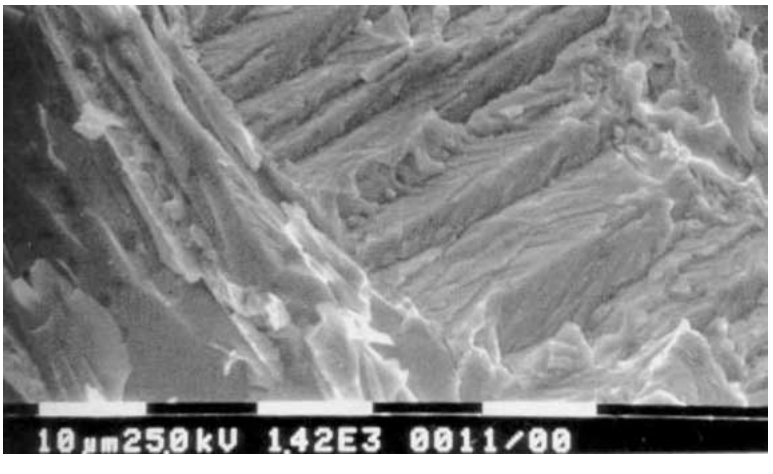

Figure 10 Secondary Electron image of Area B showing quasi-cleavage fracture.

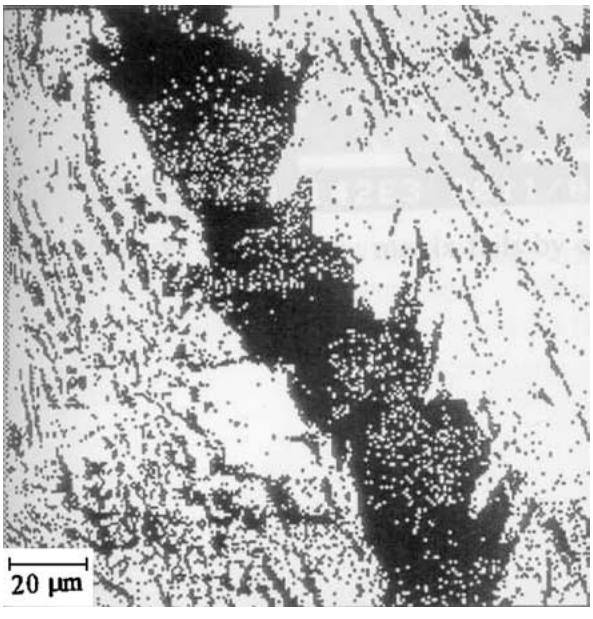

Figure 11 Cr K_α map, showing that the chromium content is concentrated in the cleavage areas of the fracture surface.

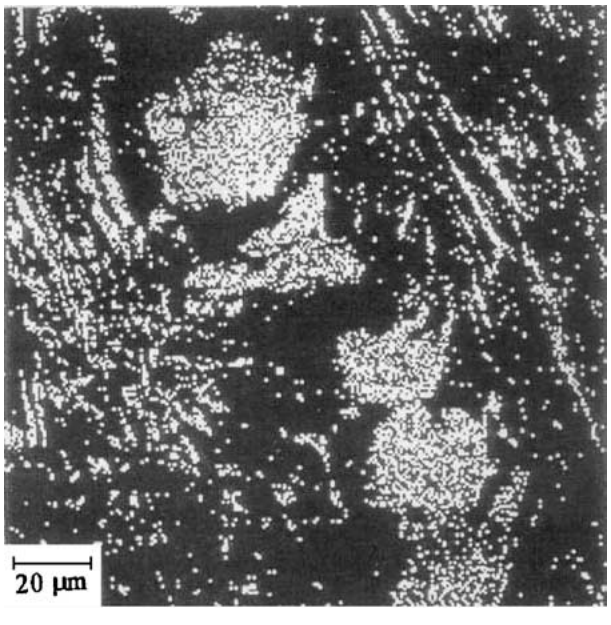

Figure 12 Fe K_α map, showing that iron is more concentrated in the quasi-cleavage fracture areas.

dissolving the mounting compound and breaking open the crack, the sample was re-photographed (Fig. 14). Comparison between Figs 13 and 14 shows that catastrophic fracture occurred in the dendrites at regions A and B.

The areas on the fracture surface corresponding to these regions can be seen in Fig. 15. Examination of this fractograph shows the regions A and B, as fracture through the austenitic dendrites, are remarkably smooth. The smoothness of the surface might be interpreted as implying cleavage fracture, but austenite, being an F.C.C material theoretically should never fail by cleavage. In any case, riverlines typical of such brittle fracture were not observed. It is theoretically possible for flat regions of a fracture surface to be produced by processes of dislocation glide rather than by brittle crack propagation if the observed plane is a shear plane. In Fig. 13 it can be observed that the plane of fracture through the dendrites is at an angle to that through the more brittle phases, supporting the idea that the austenite failed by shear.

In conclusion, it can be stated that:

(i) the eutectic carbides dominated the fracture surfaces and failed by cleavage;

(ii) the quasi-brittle fracture areas represent crack propagation through the eutectic martensite;

(iii) shear failure through the dendritic austenite appears to have occured in the reduced carbon alloys B and E.

The implication is that even though the eutectic carbide network is continuous for each alloy, reduction of the volume fraction of eutectic carbides increases the amount of crack propagation through the dendrites, thereby increasing the toughness.

TABLE V Measurement of the amount of quasi-cleavage fracture for the different alloys

Alloy	Vol% eutectic carbides	Areal% quasi-cleavage failure
A	27.1	18 ± 6
B	20.9	11 ± 6

3.5. Model of fracture

Given the extreme brittleness of the eutectic carbides, it seems extraordinary that there would be some crack propagation through the much tougher austenitic dendrites. To detail how this might occur, the concept of the characteristic distance was used.

When considering crack propagation in brittle materials, it is the distance over which the critical stress operates that is of significance. If this were not the case, then brittle materials would fail at extremely low loads, particularly in the presence of a sharp crack [13]. Thus there is a "characteristic distance" over which a critical stress must operate before crack extension occurs. In other words, it is the local microscopic stress and the microstructure directly ahead of an advancing crack which influences fracture. The characteristic distance can be calculated using the RKR fracture model. The RKR model is derived from the stress distribution ahead of a sharp crack, as determined by Rice and Johnson [33]. The stress distribution is expressed as a fraction of the yield strength and is given as a function of the "dimensionless distance" ahead of the crack tip:

$$\text{Distance from crack tip (as a function of } \sigma_x/\sigma_o) = \frac{X}{(K/\sigma_o)^2} \quad (3)$$

where X = characteristic distance, K = stress intensity factor, σ_o = the flow stress (approximated by the yield strength) and σ_x = the local stress at the crack tip (approximated by σ^F_{blunt}).

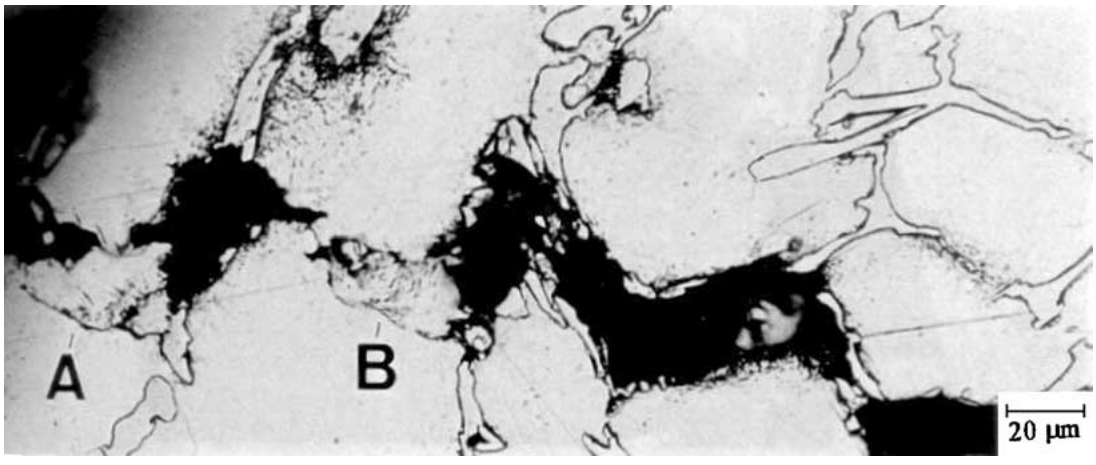

Figure 13 The crack path of a K_{Ic} sample. The test was interrupted to preserve the crack path.

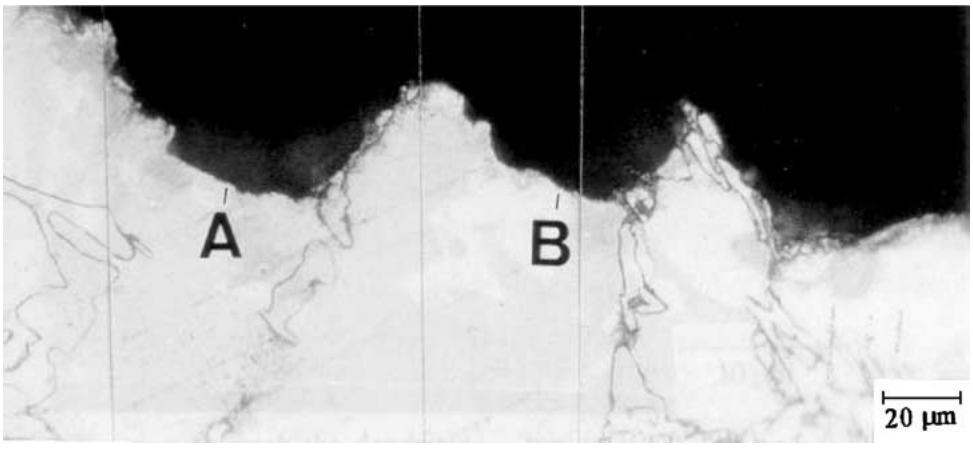

Figure 14 After photography, the crack path of Fig. 13 was broken open and re-examined under a reflected light microscope.

At fracture, the local stress at the crack tip can be derived from the blunt notch fracture strength and the analysis by Griffiths and Owen [26]. The stress intensity factor equals the fracture toughness at fracture. The flow stress can be approximated by the yield stress. Given these material properties, the characteristic distance X, can then be calculated.

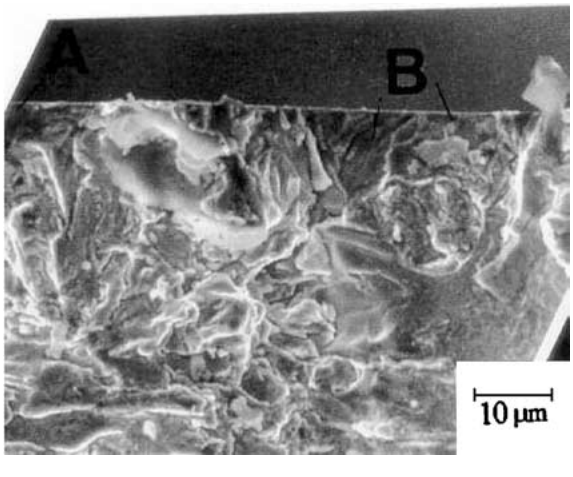

Figure 15 After photography, the crack path of Fig. 14 was removed from the mounting compound and examined in the S.E.M. (Secondary Electron Image).

3.6. Comparison of characteristic distance with microstructural properties

Table VI shows the calculated characteristic distances, X, for each alloy. For the traditional full carbon alloy A, the ratio of the fracture strength to the yield strength was so low that the characteristic distance must be smaller that the lowest value given by the Rice and Johnson stress distributions. Also shown in Table VI are measured values of the thickness of the eutectic phases.

Comparison between the microstructural features and the characteristic distances shows that the characteristic distance scales inversely with the thickness of the eutectic phases. This is in contrast to other results for steels [13] where the characteristic distance was found to be directly proportional to a microstructural feature.

Furthermore, given that the eutectic phases form a network which is continuous in three dimensions and that the deep etching experiments showed that reduction of the carbon content does not reduce this continuity, the existence of a relationship between the thickness of the eutectic phases and the characteristic distance is questionable.

In contrast, Zhou *et al.* [31] interpreted the characteristic distance as the radius which defined a volume within which it was likely that a flaw can be found. With this understanding of the characteristic distance,

TABLE VI Yield strength values for IIE-2 were taken from the literature [22]. Yield strength of E was taken to be equal to an average of the yield strengths of alloys with carbon contents on either side of its own

Alloy	%carbon	(σ_y/σ_f)	K_{Ic} (MPa$\sqrt{m}$)	X (μm)	Thickness of eutectic phases (E.P.T) (μm)	E.P.T/X	% crack propagation through the dendrites
A	2.82	1.0	25.6	<0.4	12	30	0.13 ± 0.18
B	1.86	1.2	28.5	1.1 ± 0.2	8	7.3	4.8 ± 0.8
E	1.52	1.3	32.1	1.9 ± 0.3	6.5	3.4	3.6 ± 1.9

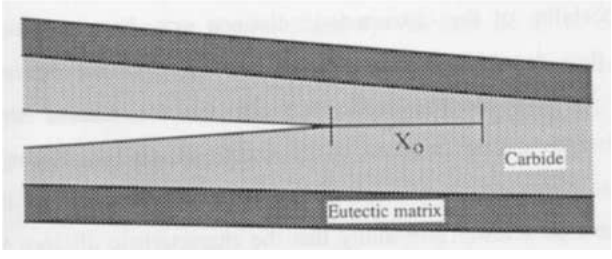

Figure 16 When the crack and the eutectic phases are aligned, fracture can be achieved completely within the eutectic phase network. X_O is the characteristic distance.

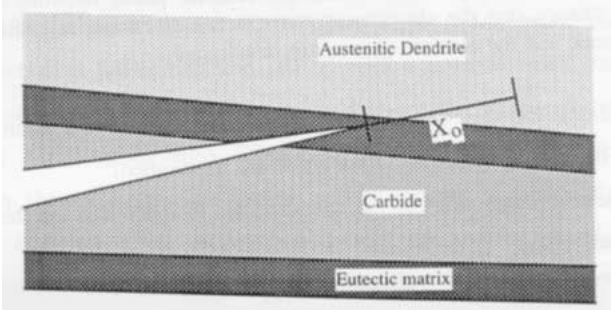

Figure 17 When the eutectic phases and the crack are misaligned, it is possible that the characteristic distance will extend into the dendritic austenite. X_O is the characteristic distance.

and assuming that cracks will initiate in the eutectic carbides, it can be seen that further crack propagation must rely on two variables:

(a) the amount of misalignment between the characteristic distance and the eutectic network;

(b) the relative sizes of the characteristic distance and the eutectic carbide network.

The amount of misalignment between the characteristic distance and the eutectic carbide network relates to the convolution of the eutectic phases. Given that the carbon content affects the amount of eutectic in any one casting, it could be assumed that as the carbon content is reduced, the convolution of the eutectic network increases. Researchers have given qualitative views that this is indeed the case [7, 11]. A more convoluted eutectic structure will increase the amount of misalignment between the crack and the carbides, thereby increasing the chance that the characteristic distance extends into the austenite (see Figs 16 and 17).

The results in Table VI show that as the carbon content is reduced from 2.8 to 1.5%, there is a ten-fold decrease in the ratio of the thickness of the eutectic phases to the characteristic distance. As these two parameters approach each other in value, the chance that the characteristic distance will extend into the dendrites once the crack and the eutectic phases are misaligned increases. Supporting this idea is the observation that as the E.P.T/X_O ratio decreases, the observed amount of crack propagation through the dendrites increases.

Thus, crack propagation into the austenitic dendrites appears to be affected by the convolution of the eutectic carbide network and the size of the eutectic "packets" relative to the characteristic distance.

Finally, thought must be given as to the type of crack propagation. Fracture can either be continuous, with cracks initiating in the eutectic carbides and then propagating through the dendrites (see Fig. 18) or the process can be discontinuous with microcracks forming ahead of the main crack front (Fig. 19).

Microstructural examination of interrupted K_{Ic} tests, show that the eutectic carbides do crack ahead of the main crack front (see Fig. 20). These cracks could

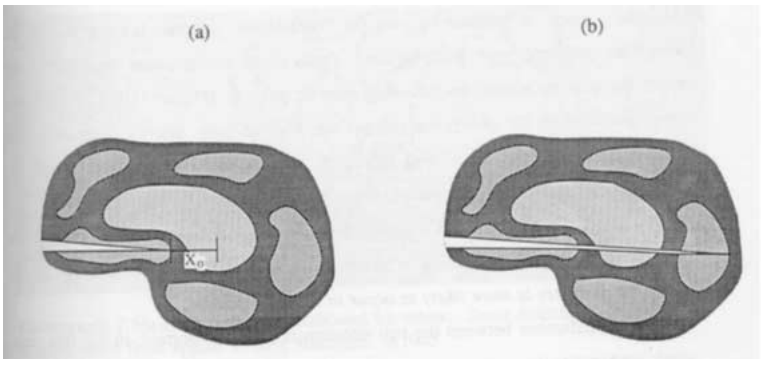

Figure 18 Crack propagation as a continuous process.

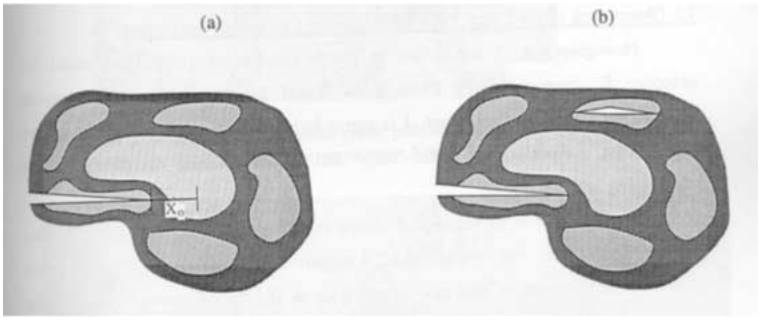

Figure 19 Crack propagation as a discontinuous process.

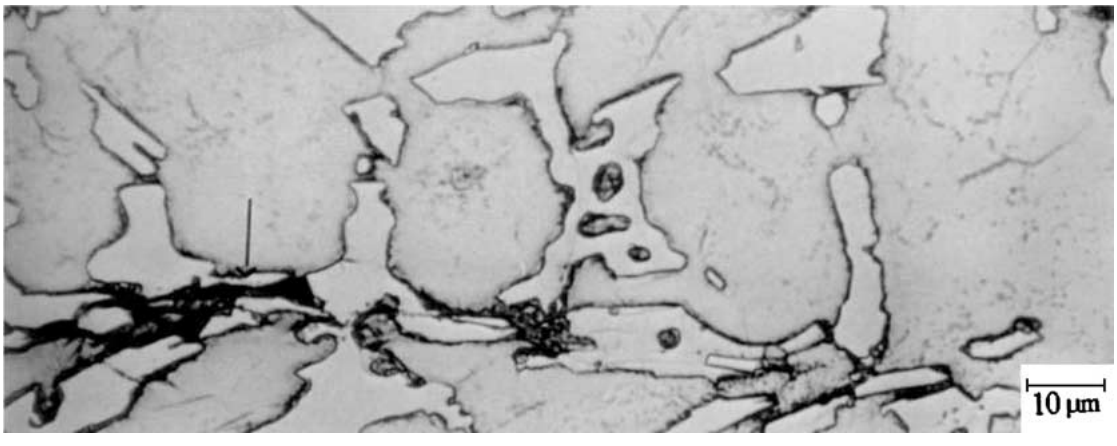

Figure 20 Cracking through the eutectic carbides. The arrow indicates the crack tip.

be produced from elastic shock waves propagating through the material and do not necessarily indicate a discontinuous fracture process. However, there were a number of cases where cracks halted at dendrites before finally fracturing through the dendritic constituent. Examples of this type of crack path is shown in Fig. 13.

4. Conclusions

It was shown that reducing the carbon content of a high chromium white cast iron does increase the as-cast fracture toughness, even though the eutectic carbide network is still continuous for all the carbon levels examined. Scanning electron microscopy and X-ray mapping was used to identify the phases on the fracture surfaces. Increases in fracture toughness were found to correlate with an increase in the amount of fracture occuring through the austenitic dendrites. The concept of the characteristic distance for brittle fracture implied that crack propagation through the dendrites occurred due to convolution of the eutectic network, when the characteristic distance was small relative to the thickness of the eutectic phases.

Acknowledgements

The authors would like to thank Mount Isa Mines for their sponsoring of this research project, Jenny Forrester and Roger Lumley for help with X-ray mapping and Bruce Crawford for his help in developing some of the diagrams.

References

1. C. P. TABRETT, I. R. SARE and M. R GHOMASHCI, *Intern. Mater. Rev.* **41** (1996) 59.
2. D. E. DEISBURG, in "Fracture Toughness and Slow Stable Cracking," Proceedings of the 1973 National Symposium on Fracture Mechanics Part I, ASTM STP 559 (ASTM, Philadelphia, 1974) p. 3.
3. M. RADULOVIC, M. FISET, K. PEEV and M. TOMOVIC, *J. Mater. Sci.* **29** (1994) 5085.
4. S. K. HANN and J. D. GATES, *ibid.* **32** (1997) 1249.
5. G. L. F. POWELL, *Metals Forum* **3** (1980) 37.
6. K. H. ZUM GAHR, *Zietschrift fur Metallkunde* **71** (1980) 103.
7. R. W. DURMAN, *The British Foundryman* **74** (1981) 45.
8. M. A. QIAN, W. C. CHANG and S. HARADA, *J. Mater. Sci.* **31** (1996) 1865.
9. S. B. BINER, *Canadian Metall. Quart.* **24** (1985) 155.
10. *Idem.*, *ibid.* **24** (1985) 163.
11. A. KOOTSOOKOS, J. D. GATES and R. A. EATON, *Cast Metals* **7** (1995), 239.
12. F. MARATRAY, *Trans. Amer. Foundr. Soc.* **79** (1971) 121.
13. R. O. RITCHIE, J. F. KNOTT and J. R. RICE, *J. Mech. Phys. Sol.* **21** (1973) 395.
14. AUSTRALIAN STANDARDS ASSOCIATION, Australian Standards, AS2027, Australian Standards Association, Australia, 1985, p. 12.
15. T. E. NORMAN, United States Patent, 4 547 221 (1985) p. 58.
16. J. SHEN and Q. D. ZHOU, *Cast Metals* **1** (1988) 79.
17. F. MARATRAY and A. POULALION, *Trans. Amer. Foundrymen's Soc.* **90** (1982) 795.
18. K. H. ZUM GAHR and W. G. SCHOLZ, *J. Metals* **32** (1980) 38.
19. AMERICAN SOCIETY FOR TESTING AND MATERIALS, Annual Book of A.S.T.M Standards, A.S.T.M E-399-90 (1990) vol. 3.01, p. 509.
20. P. N. CREPEAU and S. D. ANTOLOVICH, *Trans. Amer. Foundr. Soc.* **94** (1986) 503.
21. AMERICAN SOCIETY FOR TESTING AND MATERIALS, Annual Book of A.S.T.M Standards, A.S.T.M E562-89 (1993) Vol. 3.01, p. 612.

22. E. UNDERWOOD, "Quantitative Stereology" (Addison-Wesley Publishing Company, Massachesetts, 1970) p. 148.
23. AMERICAN SOCIETY FOR TESTING AND MATERIALS, 1993, Annual Book of A.S.T.M Standards, A.S.T.M E562-89, Vol. 3.01, p. 206.
24. G. L. F. POWELL and P. G. LLOYD, *Metallography* **14** (1981) 271.
25. G. L. F. POWELL and G. LAIRDII, *J. Mater. Sci.* **27** (1992) 29.
26. J. R. GRIFFITHS and D. R. J. OWEN, *J. Mech. Phys. Solids* **19** (1971) 419.
27. G. E. DIETER, "Mechanical Metallurgy," 3rd ed. (McGraw Hill Book Company, Singapore, 1986) p. 80.
28. A. P. GREEN and B. B. HUNDY, *J. Mech. Phys. Solids* **16** (1956) 205.
29. T. H. COURTNEY, in "Mechanical Behaviour of Materials" (McGraw-Hill Publishing Company, Singapore, 1990) p. 380.
30. J. R. RICE and M. A. JOHNSON, in "Inelastic Behaviour of Solids," edited by M. F. Kanninen *et al.* (McGraw-Hill, New York, 1970) p. 641.
31. W. ZHOU, B. VOSS and J. G. BLAUEL, *Scripta Metallurgica et Materialia* **2** (1992) 1411.

Received 17 April
and accepted 27 August 2003